Journal of Superconductivity and Novel Magnetism (2019) 32:2885–2893
https://doi.org/10.1007/s10948-019-5051-2

ORIGINAL PAPER

Mössbauer, Magnetization and Structure Characterizations of the Annealed $Sr_{1/3}Mn_{1/3}Co_{1/3}Fe_2O_4$ Ferrite Nanoparticles

Nadir S. E. Osman[1,2] · Thomas Moyo[1]

Received: 8 November 2018 / Accepted: 8 February 2019 / Published online: 7 March 2019

Abstract

$Sr_{1/3}Mn_{1/3}Co_{1/3}Fe_2O_4$ ferrite nanoparticles were synthesized by glycol thermal technique. The structure and morphology of the Nano ferrites were studied by X-ray powder diffraction, Fourier transform infrared FTIR, high-resolution scanning electron microscopy, and high-resolution transmission electron microscopy. The induced internal strains were investigated by Williamson plots. The results show mono-dispersive property of the sample and particle sizes that increase with increasing annealing temperature, T_A. The magnetic hyperfine fields were found to be sensitive to T_A as seen from room temperature ^{57}Fe Mössbauer measurements. The magnetic hysteresis loops were performed in external magnetic field of up to 50 kOe. Room temperature $M-H$ loops showed that the coercive fields increased to a maximum at T_A of 500 °C and then decreased thereafter. Significant increases in coercive fields were observed at a measuring temperature of 4 K. Distortions in the hysteresis loops at 4 K were observed where thermal annealing effect appears to induce strong linear correlation between coercive fields and saturation magnetizations.

Keywords Glycol-thermal · Annealing temperature · Mössbauer · Spin freezing · Hysteresis loops

1 Introduction

Recently, semiconductor magnetic nanomaterials have received much awareness than that of their same bulk materials, due to their size and surface effects, which exhibit unique properties such as magneto-optical, electrochemical, and photo-catalytic activities [1–6]. Cobalt ferrite with spinel structure has attracted increasing attention due to its high coercivity, moderate saturation magnetization, and high chemical stability [7, 8]. These interesting properties allow $CoFe_2O_4$ to be used in many applications such as in magneto-caloric refrigeration [3, 9], gas sensors [4, 10], ferro-fluid technology [5, 11], medical diagnostics, and magnetic resonance imaging enhancement [6, 12]. $CoFe_2O_4$ has also been reported as the best catalyst by Antony et al. [13–16]. The application of cobalt ferrite is highly affected by its magnetic behavior. The size and shape of $CoFe_2O_4$ nanoparticles play significant role in determining its magnetic properties [17]. This is associated with the method of sample preparation which can be solid state reaction or wet chemistry technique. However, synthesis by chemical methods such as sol gel, hydrothermal, and glycol-thermal techniques is preferable to produce monodispersed nanoparticles. A typical spinel ferrite has the general formula of AB_2O_4 where A and B are the atoms at tetrahedral (A) and octahedral (B) sites, respectively, and $CoFe_2O_4$ ferrite is a typical example. Double substitutions on the A site can produce materials with new properties that are different from their singularly substituted spinel derivatives. Of particular interest are compounds with equal atomic substitutions on A sites. We are interested in similar types of nanoparticle materials. Hence, the present work is extended to triple equal atomic substitutions in order to study the phase formation and thermal stability of such compounds.

The annealing process can also significantly affect the structure and morphology of the nanoparticles. Therefore, the magnetic properties are expected to vary with annealing temperature. In our previous work, we have reported

✉ Nadir S. E. Osman
nadir-shams@hotmail.com; nadirosman@sustech.edu

[1] School of Chemistry and Physics, Westville campus, University of KwaZulu-Natal, P/Bag X54001, Durban 4000, South Africa

[2] Institute of Laser, Sudan University of Science and Technology, P.O. Box 407, 11113 Khartoum, Sudan

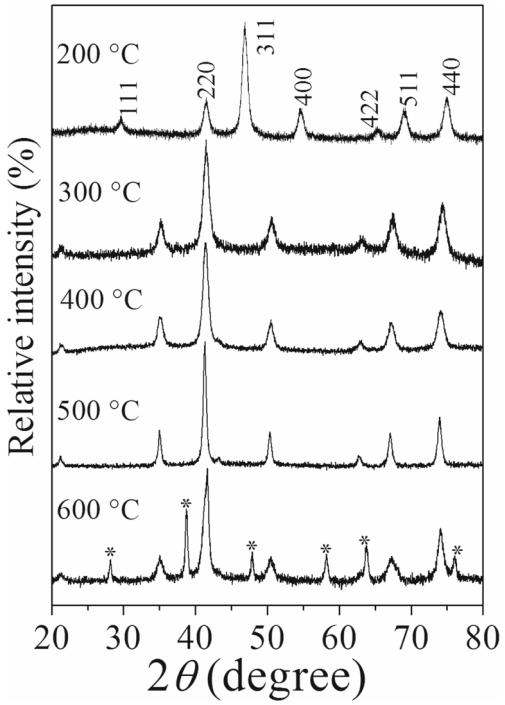

Fig. 1 XRD patterns for the as-prepared and samples annealed at different temperatures of $Sr_{1/3}Mn_{1/3}Co_{1/3}Fe_2O_4$ ferrite nanoparticles

the temperature dependence of coercivity and magnetization of $Sr_{1/3}Mn_{1/3}Co_{1/3}Fe_2O_4$ ferrite nanoparticles [18]. The current work discusses the effect of annealing temperature on structure and magnetic properties of the synthesized $Sr_{1/3}Mn_{1/3}Co_{1/3}Fe_2O_4$ ferrite nanoparticles.

Table 1 Lattice parameters (a), XRD crystallite sizes (D_{XRD}), and microstrains (ε) for the as-prepared and annealed samples of $Sr_{1/3}Mn_{1/3}Co_{1/3}Fe_2O_4$ ferrite nanoparticles

T_A (°C)	a (Å) ±0.01	D_{XRD} (nm) ±0.1	D_{HRTEM} (nm) ±2	ρ_{XRD} (g/cm^3) ±0.01	ε ±0.0003
200	8.41	10.8	9	5.41	0.0014
300	8.37	11.7	12	5.48	0.0009
400	8.39	13.2	13	5.44	0.0009
500	8.41	22.7	14	5.40	0.0009

2 Experimental Details

The $Sr_{1/3}Mn_{1/3}Co_{1/3}Fe_2O_4$ ferrite nanoparticles were produced by glycol-thermal technique using a Watlow series model PARR 4843 stirred pressure reactor. The starting materials were high purity $SrCl_26H_2O$, $MnCl_24H_2O$, $CoCl_24H_2O$, and $FeCl_26H_2O$ all purchased from Sigma-Aldrich. Stoichiometric amounts of metal chlorides were dissolved in deionized water using a magnetic stirrer for 30 min. Drops of NH_4OH were added slowly to the mixture until a pH of 9 was reached. The precipitate was washed using deionized water over a Whatman glass

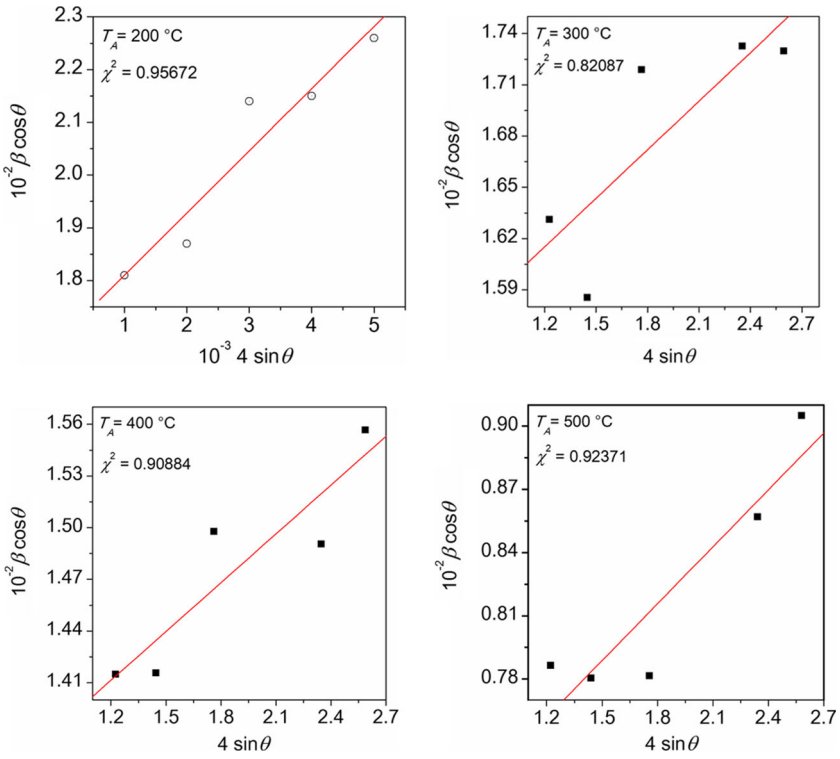

Fig. 2 Williamson-Hall plot of $\beta \cos\theta$ versus $4 \sin\theta$ for $Sr_{1/3}Mn_{1/3}Co_{1/3}Fe_2O_4$ ferrite nanoparticles

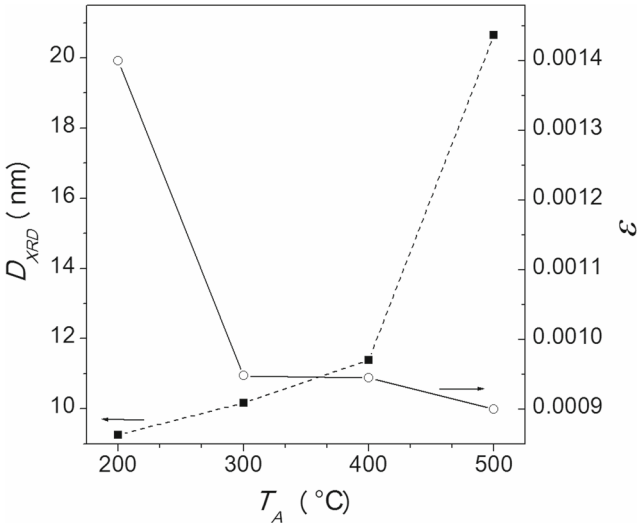

Fig. 3 Variation of crystallite size and the microstrain with annealing temperature for $Sr_{1/3}Mn_{1/3}Co_{1/3}Fe_2O_4$ ferrite nanoparticles

microfiber filter. $AgNO_3$ standard solution was used to confirm that all the chloride ions had been removed. The wet precipitate was reacted in ethylene glycol at 200 °C in a pressure reactor under continuous stirring for 6 h at a pressure of about 100 Psi. After the reaction, the mixture was washed with deionized water and then with ethanol. The final product was dried using a 200 W infra-red lamp. The dried sample was homogenized using an agate mortar and pestle. Different portions of the sample were annealed for 6 h at different temperatures (300 °C, 400 °C, 500 °C, and 600 °C) under flowing argon gas of 99.999% purity. The phase and structural characterizations of the samples were obtained by a Phillips X-ray diffractometer type Model: PAN analytical, EMPYREAN using CoKα radiation. The morphology and micro-structure of the nanoparticles were investigated by a high-resolution transmission electron microscope (HRTEM) (type: Jeol_JEM-1010) and a high-resolution scanning electron microscope (HRSEM) (Ultra Plus ZEISS-FEG HRSEM instrument). Fourier transform infra-red (FTIR) spectra of the samples were recorded with a PerkinElmer Spectrum 100 with Universal ATR sampling accessory in the range 400–4000 cm^{-1} with a resolution of 0.4 cm^{-1}. Room temperature ^{57}Fe Mössbauer spectra were obtained by a conventional spectrometer using a ^{57}Co source sealed in Rh matrix and vibrated at constant acceleration. A mini cryogen free measurement system was used to perform the magnetization measurements at 4 and 300 K in magnetic fields of up to 5 tesla.

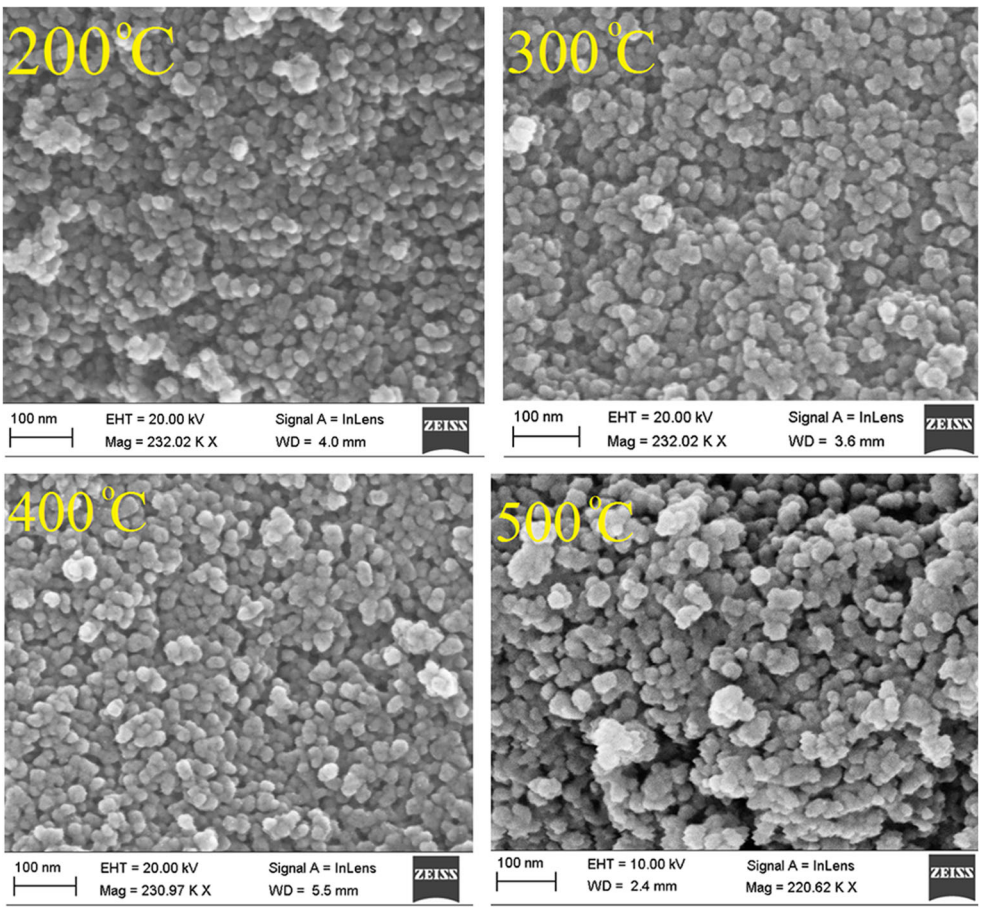

Fig 4 HRSEM images for the as-prepared and samples annealed at different temperatures of $Sr_{1/3}Mn_{1/3}Co_{1/3}Fe_2O_4$ ferrite nanoparticles

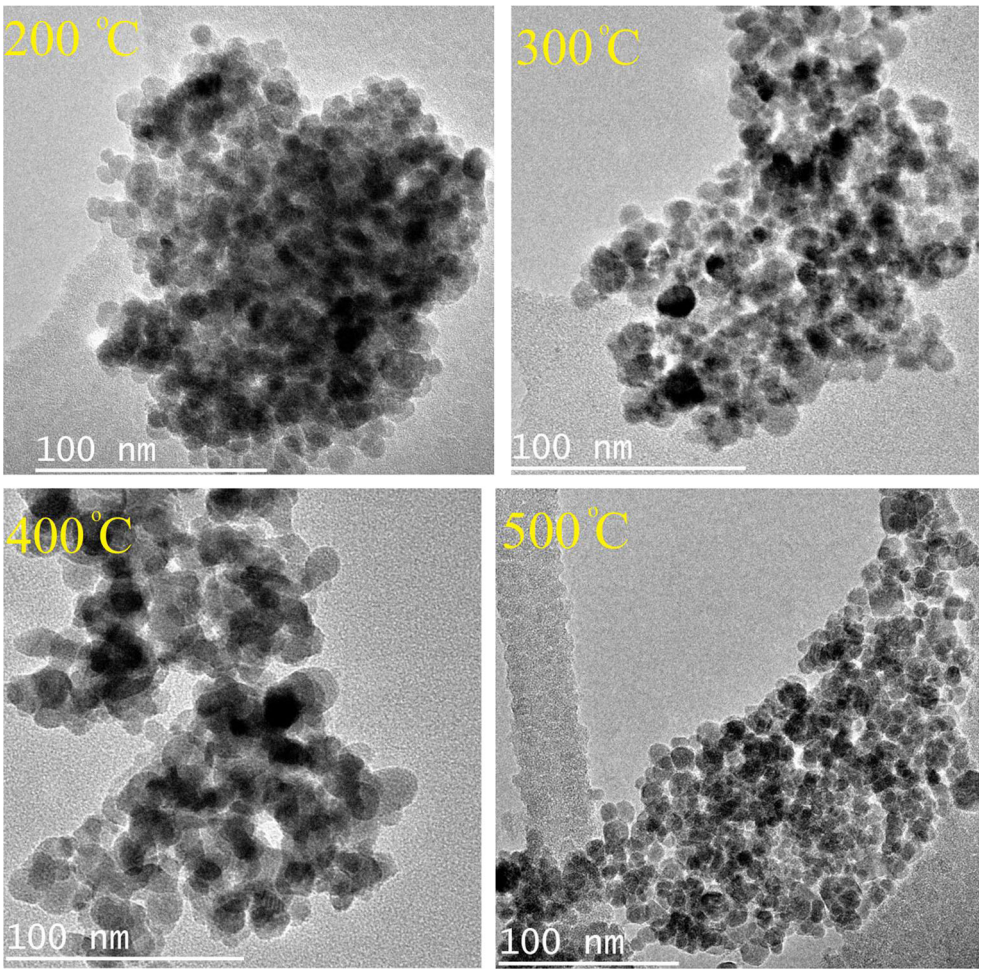

Fig. 5 HRTEM images for the as-prepared and samples annealed at different temperatures of $Sr_{1/3}Mn_{1/3}Co_{1/3}Fe_2O_4$ ferrite nanoparticles

3 Results and Discussion

Figure 1 shows X-ray diffraction (XRD) results of the as-prepared and annealed samples of $Sr_{1/3}Mn_{1/3}Co_{1/3}Fe_2O_4$ at different temperatures T_A of 300 °C, 400 °C, 500 °C, and 600 °C. It is clear that the spinel phase structure collapses at $T_A = 600$ °C. We suspect the additional peaks that appear at 600 °C to be due to an impurity phase such as α-Fe_2O_4 [19]. The lattice parameters a were calculated using Bragg's equation $a = d(h^2 + k^2 + l^2)^{1/2}$, where d is the inter-planar spacing and $hklhkl$ are the Miller indices [20]. The average XRD crystalline sizes D_{XRD} were calculated using modified Scherrer's equation $\ln\beta = \ln\frac{0.9\lambda}{D} + \ln\frac{1}{\cos\theta}$, where β is the full-width at half-maximum and θ is the Bragg's angle [21]. The microstrains of the annealed samples were investigated based on the Williamson-Hall plots as shown in Fig. 2. The values of the lattice parameter, crystallite size, and lattice-strain ε for the as-prepared and the annealed samples of $Sr_{1/3}Mn_{1/3}Co_{1/3}Fe_2O_4$ at different temperatures are given in Table 1. The lattice parameters decreased slightly after annealing at $T_A = 300$ °C and subsequently increased with increasing T_A. The as-prepared sample appears to be more strained due to the initial synthesis conditions. Hence, annealing leads initially to internal thermal relaxation that causes a drop in the lattice parameter followed by an increase. The crystallite sizes increase from 9.3 ± 0.1 to 20.6 ± 0.1 nm with increase in annealing temperature from 200 to 500 °C, respectively. The crystallite size increased with increasing temperature. This can be attributed to the coalescence effect due to additional crystallites merging at higher temperature [22–25]. The microstrain ε values decrease from 0.0014 ± 0.0002 to 0.0009 ± 0.0002 as T_A increases from 200 to 500 °C, respectively. We attribute decreases in ε values to the reduction of defects and internal stresses [26]. Figure 3 shows the variation of crystallite size and microstrain with annealing temperature.

The morphology of the as-prepared and annealed samples was investigated by HRSEM and HRTEM as displayed in Figs. 4 and 5, respectively. The particle sizes increase as the annealing temperatures increase.

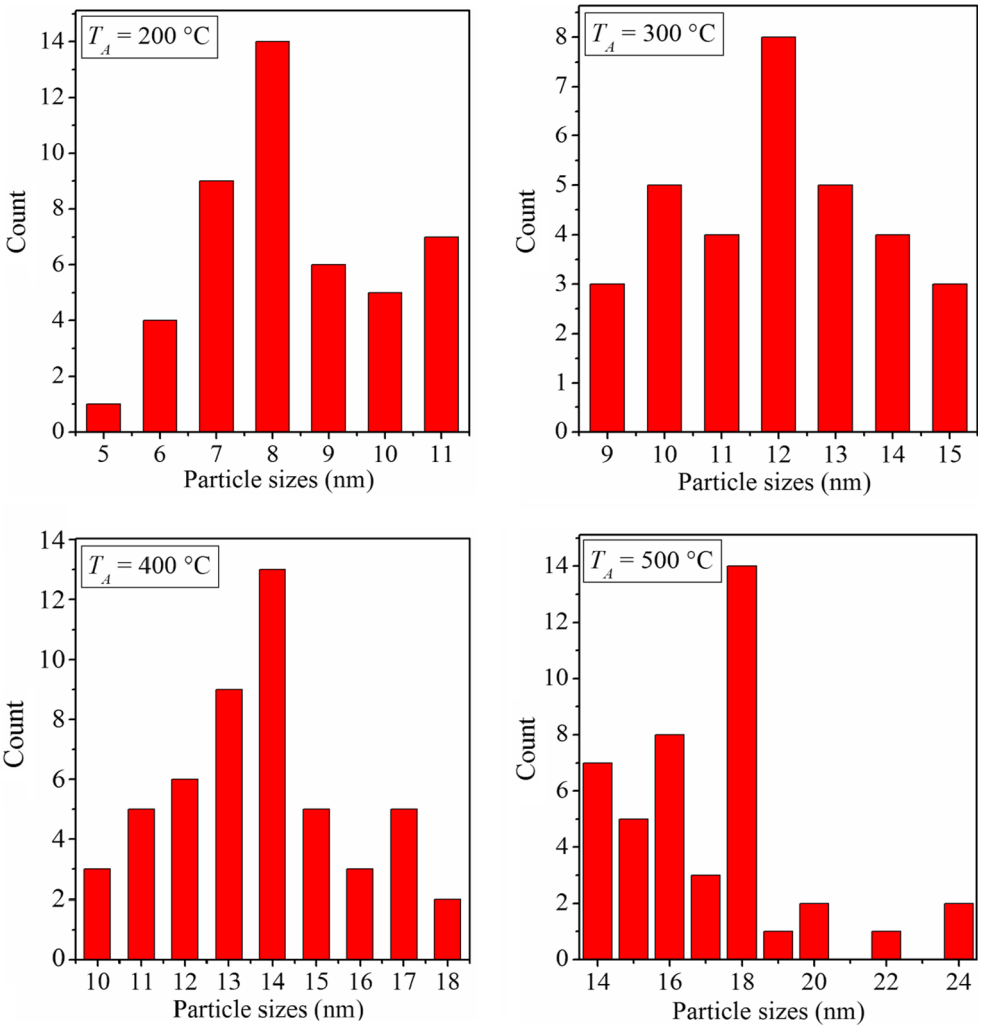

Fig. 6 Sizes distributions for $Sr_{1/3}Mn_{1/3}Co_{1/3}Fe_2O_4$ ferrite nanoparticles annealed at different temperatures

However, the annealed nanoparticles appear to have more regular shapes with a narrow particle size distribution. Figure 6 shows the size distribution for annealed samples of $Sr_{1/3}Mn_{1/3}Co_{1/3}Fe_2O_4$ at different temperatures.

Figure 7 shows the FTIR spectra analyses for the as-prepared and the annealed samples of $Sr_{1/3}Mn_{1/3}Co_{1/3}Fe_2O_4$ at different temperatures. The patterns confirm the spinel structure of the samples which are supported by the XRD results. The peaks at 563, 539, and 548 cm^{-1} are attributed to stretching vibrations of Fe^{3+}-O^{2-} in the samples [27]. The adsorbed water featured by bands at 3016, 3017, and 3286 cm^{-1} are assigned to O–H stretching vibration, whilst 1229, 1366, 1585, and 1739 cm^{-1} are assigned to H–O–H bonding modes of vibration.

Room temperature ^{57}Fe Mössbauer spectra for the as-prepared and annealed $Sr_{1/3}Mn_{1/3}Co_{1/3}Fe_2O_4$ ferrite nanoparticles are shown in Fig. 8. The spectra were fitted with two Zeeman sextets. This is associated with Fe ions in tetrahedral A and octahedral B sites. The magnetic hyperfine parameters obtained from the fitted spectra are shown in Table 2. The deduced values of isomer shifts δ confirm that only Fe^{3+} ions are present in the samples. Hence, it can be concluded that the oxidation state of Fe ions has not been changed by the annealing process. However, the isomer shifts slightly change with increasing the annealing temperature. This can be attributed to a small change in s-electron density of the sample, associated with the grain growth. The obtained values of magnetic hyperfine fields indicate a strong super-exchange interaction between magnetic moments. The higher values of magnetic hyperfine fields are expected to be at octahedral B sites. This is due to the dipolar field that is associated with the deviation from the cubic symmetry and covalent nature of Fe^{3+}–O^{2-} bonds at tetrahedral A site [28]. Figure 9 shows the variation with T_A of magnetic hyperfine fields H_A and H_B.

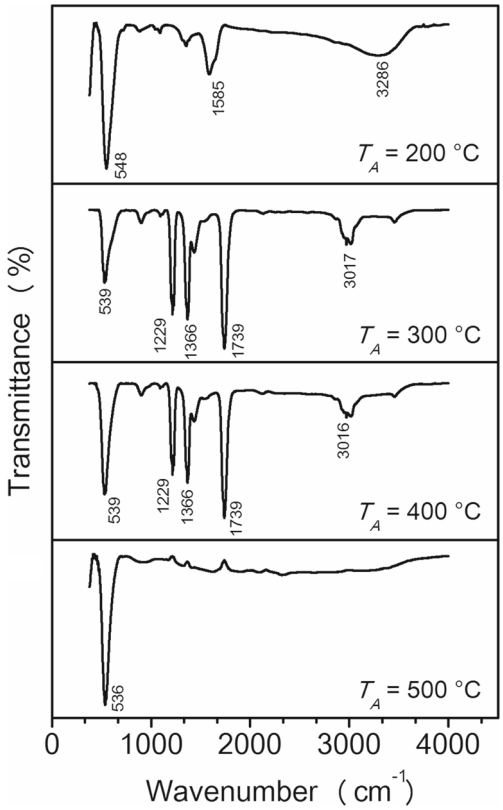

Fig. 7 FTIR spectra of spectra for $Sr_{1/3}Mn_{1/3}Co_{1/3}Fe_2O_4$ ferrite nanoparticles annealed at different temperatures

On A site, we observed an initial reduction at T_A = 300 °C followed by an increase in H_A at higher T_A. At

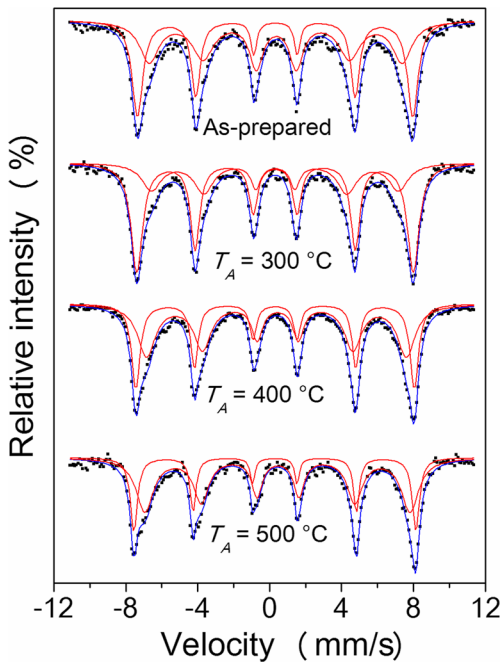

Fig. 8 Room temperature ^{57}Fe Mössbauer spectra for the as-prepared and samples annealed at different temperatures of $Sr_{1/3}Mn_{1/3}Co_{1/3}Fe_2O_4$ ferrite nanoparticles

Table 2 Isomer shifts (δ), hyperfine magnetic fields (H), line widths (Γ), and Fe^{3+} fraction population (f) on A-site and B-site for the as-prepared and samples annealed at different temperatures of $Sr_{1/3}Mn_{1/3}Co_{1/3}Fe_2O_4$ ferrite nanoparticles

T_A (°C)	δ (mm/s)		H (kOe)		Γ (mm/s)		f (%)	
	δ_A ± 0.02	δ_B ± 0.02	H_A ± 9	H_B ± 4	Γ_A ± 0.08	Γ_B ± 0.1	f_A ± 5	f_B ± 7
200	0.36	0.32	436	475	0.46	0.20	53	47
300	0.31	0.31	426	477	0.32	0.29	34	66
400	0.42	0.31	448	480	0.37	0.23	59	41
500	0.45	0.29	457	487	0.36	0.15	68	33

octahedral B sites,H_B increases from 475 ± 2 to 487 ± 1 kOe as T_A increased from 200 to 500 °C, respectively. The increase in magnetic hyperfine field values with annealing temperature is associated with the increase in the particle sizes. This can be attributed to the decrease in the relaxation time as shown in Néel's equation $\tau = \tau_0 \exp(-KV/k_BT)$, where V is the particle's volume and K is the anisotropy energy density [29]. The line widths were also affected by the annealing process on both tetrahedral A and octahedral B sites.

Room temperature $M-H$ loops for the as-prepared and annealed samples of $Sr_{1/3}Mn_{1/3}Co_{1/3}Fe_2O_4$ ferrite nanoparticles are shown in Fig. 10. The obtained results of magnetization M_S, coercive field H_C, remnant magnetization M_r, and squareness ratio M_r/M_S are presented in Table 3. The magnetization increased from 67.5 ± 0.4 to 71.9 ± 0.4 emu/g as the annealing temperature increased from 200 to 500 °C. The variation of M_S and H_C with T_A

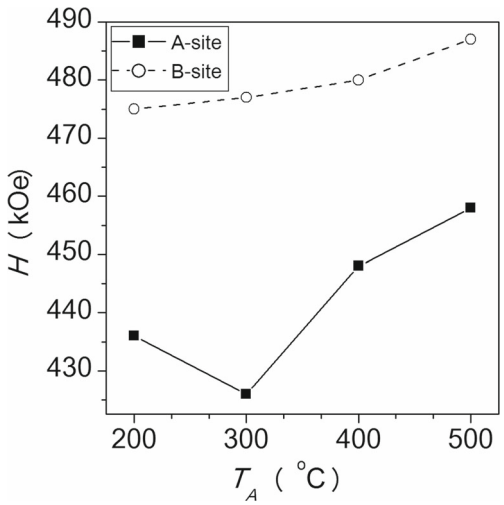

Fig. 9 Variation of hyperfine fields H_A and H_B with the annealing temperature for $Sr_{1/3}Mn_{1/3}Co_{1/3}Fe_2O_4$ ferrite nanoparticles

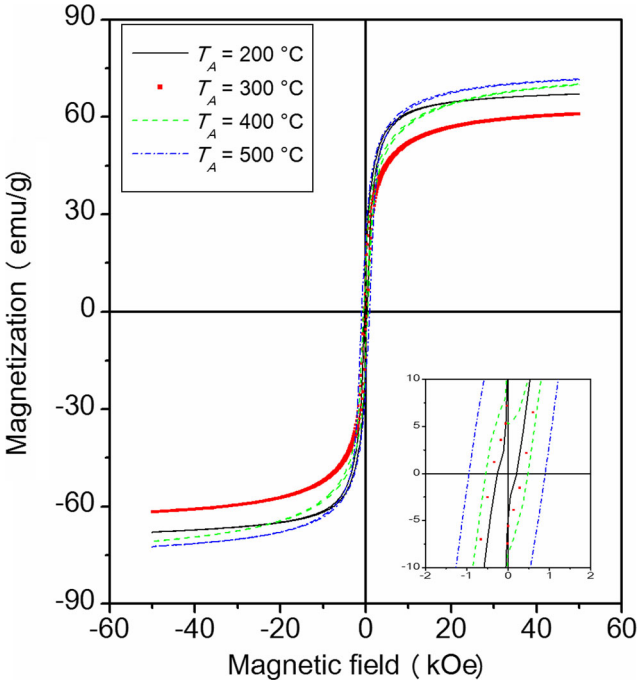

Fig. 10 Room temperature hysteresis loops for the as-prepared and samples annealed at different temperatures of $Sr_{1/3}Mn_{1/3}Co_{1/3}Fe_2O_4$ ferrite nanoparticles

Table 3 Magnetic parameters obtained at room temperature for the as-prepared and samples annealed at different temperatures of $Sr_{1/3}Mn_{1/3}Co_{1/3}Fe_2O_4$ ferrite nanoparticles

T_A (°C)	M_S (emu/g) ± 0.4	H_C (kOe) ± 0.02	M_r (emu/g) ± 1	M_r/M_S ± 0.01
200	67.46	0.24	8	0.12
300	61.29	3.88	8	0.13
400	70.39	5.10	12	0.17
500	71.94	9.22	20	0.28

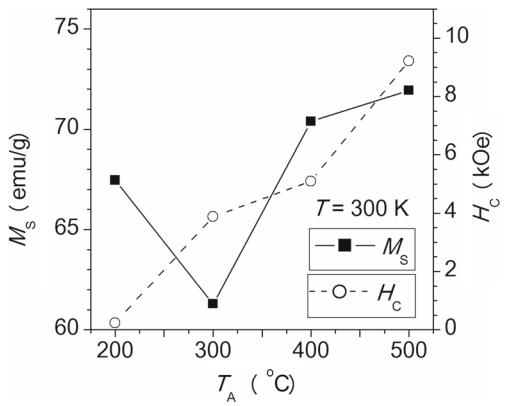

Fig. 11 Variation of M_S and H_C with T_A for $Sr_{1/3}Mn_{1/3}Co_{1/3}Fe_2O_4$ ferrite nanoparticles measured at 300 K

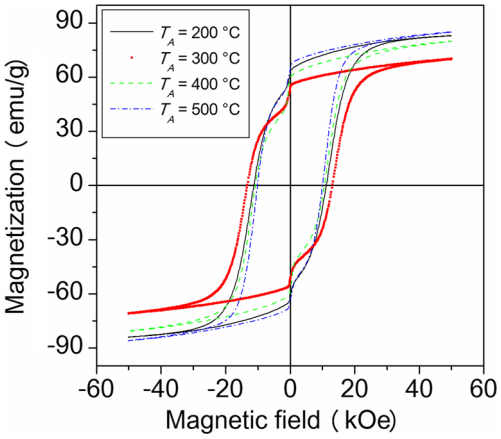

Fig. 12 Hysteresis loops of the as-prepared and annealed samples of $Sr_{1/3}Mn_{1/3}Co_{1/3}Fe_2O_4$ ferrite nanoparticles

measured at 300 K is shown in Fig. 11. It is observed that M_S value drops at 300 °C. This might be due to spin surface disorder. The coercive field increases to a maximum value at 500 °C and subsequently decreased at 600 °C. The variation of coercivity with particle sizes can be explained based on domain theory [30]. The increase of particle sizes leads to the increase of the coercivity to the maximum value at the single domain size. As the particle sizes become larger than the single domain size, the coercivity decreases [31]. The values of squareness increased from 0.12 to 0.28 by increasing the annealing temperature from 200 to 500 °C. Figure 12 shows the $M-H$ loops measured at 4 K for the as-prepared and annealed samples of $Sr_{1/3}Mn_{1/3}Co_{1/3}Fe_2O_4$ ferrite nanoparticles. The hysteresis loops of the samples at 4 K reveal large values of coercive fields (see Table 4) compared to 300 K. This indicates that the samples become magnetically harder at low temperature. We attribute this to spin freezing effect. Evidence of frozen spins at 4 K can be seen also from the distortion on the hysteresis loops [32]. In Fig. 13, we show plots of the coercive fields and saturation magnetizations at 4 K. In addition, we find a strong and interesting correlation between the coercive fields and saturation magnetizations

Table 4 Magnetic parameters obtained at 4 K for the as-prepared and samples annealed at different temperatures of $Sr_{1/3}Mn_{1/3}Co_{1/3}Fe_2O_4$ ferrite nanoparticles

T_A (°C)	M_S (emu/g) ± 1	H_C (kOe) ± 0.4	M_r (emu/g) ± 1	M_r/M_S ± 0.01
200	83	11.2	61	0.73
300	70	13.2	53	0.76
400	80	11.0	58	0.73
500	85	10.0	64	0.75

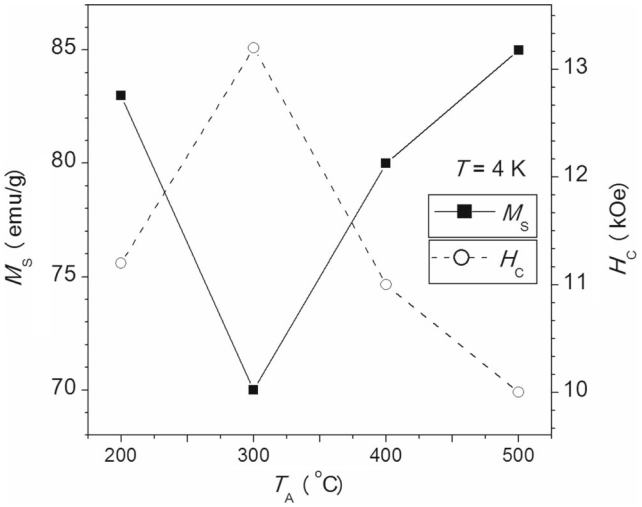

Fig. 13 Variation of M_S and H_C with T_A for $Sr_{1/3}Mn_{1/3}Co_{1/3}Fe_2O_4$ ferrite nanoparticles measured at 4 K

as illustrated in Fig. 14. This suggests a relationship of the form $H_C = H_{C0}(1 - M_S/M_0)$ induced by thermal annealing effect where H_{C0} and M_0 are constants.

4 Conclusions

The synthesized $Sr_{1/3}Mn_{1/3}Co_{1/3}Fe_2O_4$ ferrite nanoparticle sample was annealed at different temperatures of 300 °C, 400 °C, 500 °C, and 600 °C. The phase structure was confirmed by X-ray powder diffraction. The annealing temperature increased the crystallite sizes and reduced the internal strain of the sample. High-resolution scanning electron microscopy and high-resolution transmission electron microscopy images reveal that the samples have regular shape and sizes. The results also show that the particle sizes increase with increasing annealing temperature. Room temperature ^{57}Fe Mössbauer measurements show that the internal hyperfine fields increase as T_A increases. The magnetization increased from 67.5 ± 0.4 to 71.9 ± 0.4 emu/g as T_A increased from 200 to 500 °C, respectively. At room temperature, the coercive fields increased from 0.24 ± 0.03 to 9.2 ± 0.03 kOe, respectively. At 4 K, the samples became magnetically harder with distortions in the hysteresis loops which can be attributed to spin freezing effect. Increased coercivity with annealing temperature can be associated with transformation from single domain to multi-domain structure. Significant changes in the XRD patterns were observed after thermal annealing. This is also consistent with change in the FTIR spectrum for the as-prepared sample that is significantly different. We also found a strong linear correlation between the coercive fields and saturation magnetization with increased annealing temperature but not with the as-prepared sample.

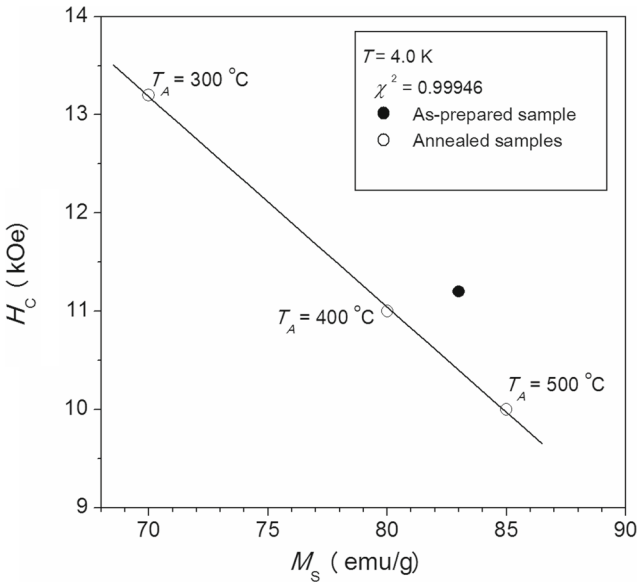

Fig. 14 Correlation between coercive fields H_C and saturation magnetizations M_S measured at 4 K for the as-prepared and annealed samples of $Sr_{1/3}Mn_{1/3}Co_{1/3}Fe_2O_4$ ferrite nanoparticles

Funding information This work was supported by the National Research Foundation (NRF) of South Africa for the equipment grant for the cryogen free measurement system.

References

1. Abraham, A.G., Manikandan, A., Manikandan, E., Jaganathan, S.K., Baykal, A., Renganathan, P.S.: J. Nanoelectron. Optoelectron. **12**, 1326 (2017)
2. Manikandan, A., Durka, M., AmuthaSelvi, M., Antony, S.A.: J. Nanosci. Nanotechnol. **16**, 448 (2016)
3. Mary Jacintha, A., Manikandan, A., Chinnaraj, K., Arul Antony, S., Neeraja, P.: J. Nanosci. Nanotechnol. **15**, 9732 (2015)
4. Hema, E., Manikandan, A., Karthika, P., Durka, M., Antony, S.A., Venkatraman, B.R.: J. Nanosci. Nanotechnol. **16**, 7325 (2016)
5. Hema, E., Manikandan, A., Gayathri, M., Durka, M., Antony, S.A., Venkatraman, B.R.: J. Nanosci. Nanotechnol. **16**, 5929 (2016)
6. Suguna, S., Shankar, S., Jaganathan, S.K., Manikandan, A.: J. Supercond. Nov. Magn. **30**, 691 (2017)
7. Mosivand, S., Kazeminezhad, I.: RSC Adv. **5**, 14796 (2015)
8. Chia, C.H., Zakaria, S., Yusoff, M., Goh, S.C., Haw, C.Y., Ahmadi, S., Huang, N.M., Lim, H.N.: Ceram. Int. **36**, 605 (2010)
9. Varma, P.C.R., Manna, R.S., Banerjee, D., Varma, M.R., Suresh, K.G., Nigam, A.K.: J. Alloys Compd. **453**, 298 (2008)
10. Xiangfeng, C., Dongli, J., Yu, G., Chenmou, Z.: Sensors Actuators B Chem. **120**, 177 (2006)
11. Kim, Y.I., Kim, D., Lee, C.S.: Phys. B Condens. Matter. **337**, 42 (2003)
12. Kang, J., Lee, H., Kim, Y.N., Yeom, A., Jeong, H., Lim, Y.T., Hong, K.S.: Nanoscale Res. Lett. **8**(1), 376 (2013)

13. Manikandan, A., Sridhar, R., Arul Antony, S., Ramakrishna, S.: J. Mol. Struct. **1076**, 188 (2014)
14. Manikandan, A., Durka, M., Arul Antony, S.: J. Supercond. Nov. Magn. **27**, 2841 (2014)
15. Hema, E., Manikandan, A., Karthika, P., Antony, S.A., Venkatraman, B.R.: J. Supercond. Nov. Magn. **28**, 2539 (2015)
16. Manikandan, A., Durka, M., Antony, S.A.: J. Supercond. Nov. Magn. **28**, 2047 (2015)
17. Zi, Z., Sun, Y., Zhu, X., Yang, Z., Dai, J., Song, W.: J. Magn. Magn. Mater. **321**, 1251 (2009)
18. Osman, N.S.E., Moyo, T.: J. Supercond. Nov. Magn. **29**, 361 (2015)
19. Thang, P.D., Rijnders, G., Blank, D.H.A.: J. Magn. Magn. Mater. **295**, 251 (2005)
20. Houshiar, M., Zebhi, F., Razi, Z.J., Alidoust, A., Askari, Z.: J. Magn. Magn. Mater. **371**, 43 (2014)
21. Monshi, A., Foroughi, M.R., Monshi, M.R.: World J. Nano. Sci. Eng. **2**(3), 154–160 (2012)
22. Silambarasu, A., Manikandan, A., Balakrishnan, K.: J. Supercond. Nov. Magn. **30**, 2631 (2017)
23. Asiri, S., Sertkol, M., Güngüneş, H., Amir, M., Manikandan, A., Ercan, İ., Baykal, A.: J. Inorg. Organomet. Polym. Mater. **28**, 1587 (2018)
24. Manikandan, A., Hema, E., Durka, M., Seevakan, K., Alagesan, T., Arul Antony, S.: J. Supercond. Nov. Magn. **28**, 1783 (2015)
25. Manikandan, A., Saravanan, A., Arul Antony, S., Bououdina, M.: J. Nanosci. Nanotechnol. **15**, 4358 (2015)
26. Rupp, J.L.M., Infortuna, A., Gauckler, L.J.: Acta Mater. **54**, 1721 (2006)
27. Kumar, L., Kumar, P., Narayan, A., Manoranjan: Int. Nano. Lett. **3**, 8 (2013)
28. Lakshman, A., Subba Rao, P.S.V., Rao, K.H.: Mater. Lett. **60**(7), 7 (2006)
29. Gabbasov, R., Polikarpov, M., Cherepanov, V., Chuev, M., Mischenko, I., Lomov, A., Wang, A., Panchenko, V.: J. Magn. Magn. Mater. **380**, 111 (2015)
30. Müller, R., Schüppel, W.: J. Magn. Magn. Mater. **155**, 110 (1996)
31. Leslie-Pelecky, D.L., Rieke, R.D.: Chem. Mater. **8**, 1770 (1996)
32. Upadhyay, C., Verma, H.C., Sathe, V., Pimpale, A.V.: J. Magn. Magn. Mater. **312**, 271 (2007)